Available online at https://link.springer.com/journal/42241
http://www.jhydrodynamics.com
Journal of Hydrodynamics, 2019, 31(4): 682-699
https://doi.org/10.1007/s42241-018-0123-5

Numerical investigation of edge configurations on piston-modal resonance in a moonpool induced by heaving excitations *

Sheng-chao Jiang[1, 2, 3], Pei-wen Cong[2, 3], Lei Sun[1], Chang-feng Liu[4]
1. *School of Naval Architecture, State Key Laboratory of Structural Analysis for Industrial Equipment, Dalian University of Technology, Dalian 116024, China*
2. *State Key Laboratory of Coastal and Offshore Engineering, Dalian University of Technology, Dalian 116024, China*
3. *Department of Civil and Environmental Engineering, National University of Singapore, Singapore*
4. *College of Ocean and Civil Engineering, Dalian Ocean University, Dalian 116023, China*

(Received June 19, 2017, Revised March 30, 2018, Accepted March 30, 2018, Published online October 26, 2018)

Abstract: The renormalization group (RNG) turbulent model is used to investigate the fluid resonance in a moonpool formed by two identical rectangular hulls under synchronous heaving excitation (e.g., a catamaran or dual pontoon). The numerical model is validated against the available experimental data, and accurate numerical solutions are obtained. The present study focuses on the amplitude of the moving hulls and the edge configuration of the moonpool entrance, as well as their influences on the piston-modal resonant wave in the moonpool. The dependence of the resonant wave amplitude in the moonpool on the heaving amplitude, the characteristic moonpool dimensions and the local velocity magnitude is derived based on a theoretical analysis, and the results are in good agreement with the RNG turbulent solutions. Five different edge profiles are considered, including two convex edges, two concave edges (both with various dimensions), and a sharp edge. Numerical examinations show that the edge configuration has a significant influence on the piston-modal resonant responses, a larger opening size leading to a higher resonant frequency and a larger resonant wave amplitude in the moonpool. Various flow patterns of the piston-modal resonance in the vicinity of the moonpool entrance are also identified, mainly depending on the edge profile. More intensive turbulent and vortical flows give rise to more significant dissipation, accounting for the smaller relative wave amplitude in the moonpool. With the increase of the heaving amplitude, the relative piston-modal resonant amplitude is decreased in an approximate power function. Within the scope of this work, the numerical investigations show that the piston-modal resonant frequency is hardly affected by the heaving amplitude.

Key words: Moonpool, wave resonance, corner shape, renormalization group (RNG) turbulent model, heaving motion

Introduction

In marine and offshore operations, the moonpool is often used to lower or lift devices, such as the pipe laying or for the diver recovery by passing through a moonpool of drilling ships, the spar platform and floating production storage and offloading (FPSO) system. The fluid resonance in the moonpool can be excited by the incident wave and/or the structure motion, with a considerable amplification of the free surface oscillation. This is a threat for the safety of the maritime structure, and the possible sea operations would be limited. The similar fluid resonance may also happen in the narrow gap between multi-hull vessels, ships in front of a gravity wharf.

Early studies of the resonant response were focused on the wave actions on simplified fixed bodies in proximity, leaving a moonpool or a narrow gap between them. Saitoh et al.[1], Peric and Swan[2] conducted experimental investigations in a wave flume, and suggested that the resonant frequency and the resonant wave amplitude are dependent on the body draft, the moonpool/gap width and the number of boxes. Numerical investigations in the frame of the potential flow theory were conducted by Faltinsen et al.[3], Sun et al.[4], Feng and Bai[5] and Li and Zhang[6], among others. It was shown that the potential flow model can be used to reasonably predict the resonant frequency and the wave amplitude outside a certain band of the resonant condition. However, around the

* Project supported by the National Natural Science Foundation of China (Grant Nos. 51490673, 51679035).
Biography: Sheng-chao Jiang (1984-), Male, Ph. D., Associate Professor, E-mail: jiangshengchao@foxmail.com
Corresponding author: Lei Sun,
E-mail: sunlei@dlut.edu.cn

resonant frequency, with the potential flow models, much larger wave amplitude is predicted than the laboratory observations. In order to make up this deficiency, various damping terms are introduced into the potential flow model[7-9]. Although accurate results can be obtained if the damping coefficients are successfully calibrated by using available experimental data, the physical meaning of the damping term remains an open question. Alternatively, numerical simulations based on the Navier-Stokes equations were carried out[10-12] and satisfactory predictions of both the resonant frequency and the resonant amplitude were obtained. However, they involve an extremely huge amount of computation even in two-dimensional cases since the direct numerical simulation (DNS) requires very fine computational meshes. The use of turbulent models instead of the DNS technique seems to be a feasible approach at present for the real high Reynolds number flow.

A variety of experimental and numerical investigations were also conducted in the cases of moving floating structures with confined moonpools, for example, the experimental work by Yang and Kwon[13] for the moonpool problem and Zhao et al.[14] for two side-by-side barges in irregular waves. The three dimensional numerical modelling in the time-domain for twin floating boxes by Zhu et al.[15] suggested again the over-predictions of the responses by the potential flow theory. In order to improve the numerical accuracy but not significantly increase the amount of computations, some coupling numerical strategies were advanced recently. Elie et al.[16] adopted the approach of the Spectral Wave Explicit Navier-Stokes Equations (SWENSE), which is a combination of the linear potential flow model in the frequency domain and a Reynolds averaging Navier-Stokes (RANS) model for the viscous flow for radiation waves, to simulate the gap resonance between side-by-side barges. The numerical results in regular waves are in agreement with experimental data. On the other hand, Fredriksen et al.[17] established a different coupling model based on the idea of domain decompositions. The laminar Navier-Stokes equations were solved by the finite volume method (FVM) for the lower region of the moonpool while the potential flow model is used in the upper region of the moonpool and the outer region based on a high-accuracy harmonic polynomial cell (HPC) method. The advantages of coupling models in the computational efficiency are obvious but the theoretical inconsistence between the potential flow model and the viscous fluid model should be kept in mind. The previous studies show that the vortical flows around the moonpool corner and inside the moonpool play a very important role in controlling the resonant response. And the vortical flows of viscous fluids might be highly dependent on the edge configuration and the motion amplitude. These aspects are generally due to the nonlinear damping effects. Kristiansen and Faltinsen[18] studied the piston-modal wave resonance in the gap formed by a ship model arranged in front of a vertical wall, with a special focus on the viscous damping caused by the flow separation from the bilge keels. The experimental and inviscid vortex tracking numerical results suggest that the viscous damping must not be neglected. Jiang et al.[19-21] computed the reflection coefficient K_r, the transmission coefficient K_t, and an integral comprehension of energy dissipation can be revealed according to the variation of the energy loss coefficient $K_l = 1 - K_r^2 - K_t^2$ with respect to incident wave frequency and amplitude. Tan et al.[22] established a viscous damping model for piston-model resonance based on a simplified equation of fluid motion in a moonpool or the narrow gap formed by two fixed boxes. The model can take into account the damping induced by box flow separation and wall friction. In another work by Kristiansen and Faltinsen[23], the piston-modal resonant behaviors in a moonpool induced by the heaving motion was investigated experimentally and numerically. A local discrete-vortex method (DVM) was adopted to simulate the vortex motion around the moonpool entrance. However, it was found that the vortex shedding is small in accordance with their test conditions, and the discrepancy between the potential solutions and the experiment observations was attributed to the nonlinearity of the free surface as the heave motion is relatively small. It is speculated that with the increase of the heaving amplitude, the wave nonlinearity and the vortex motion may become more significant. Experimental and numerical investigations were further conducted by Fredriksen et al.[17] by considering a 2-D heaving box sections with a moonpool in the middle heaving in a wave flume at a low forward speed. Two different edge shapes, i.e., the sharp shape and the convex corner shape, were tested with various heaving amplitudes. The influences of the edge configuration and the heaving amplitude on the resonant responses were shown and compared with the numerical results based on the coupling HPC potential model and the laminar Navier-Stokes solver. It was reported that the damping is increased from the sharp edge profiles to the convex edge profiles, leading to the decrease of the relative wave amplitude in the moonpool.

The present study is to further explore the influence of the edge configuration on the piston modal resonance by both widening and narrowing the moonpool entrance with respect to the standard sharp right corner. The hydrodynamic behaviors in the moonpool are examined not only in terms of the

change of the edge configuration but also the variation of the heaving amplitudes. The vortical flow in the vicinity of the moonpool entrance, which is expected to greatly affect the resonant responses, will be analyzed in the context of the turbulent flows by using the Renormalization group (RNG) turbulence simulations.

1. Numerical models

1.1 *Viscous turbulent model*

The governing equations of the incompressible turbulent flows with the RNG model in an arbitrary Lagrangian-Eulerian (ALE) reference system can be expressed as follows:

$$\frac{\partial \rho u_i}{\partial x_i} = 0 \tag{1}$$

$$\frac{\partial \rho u_i}{\partial t} + \frac{\partial \rho (u_j - u_j^m) u_i}{\partial x_j} = \rho f_i - \frac{\partial p}{\partial x_i} + \mu_e \frac{\partial}{\partial x_j}\left(\frac{\partial u_i}{\partial x_j} + \frac{\partial u_j}{\partial x_i}\right) \tag{2}$$

where u_i is the velocity component in the i-th direction, u_j^m the velocity component due to the mesh deformation in the ALE frame, p the pressure, ρ the fluid density, f_i the external body force, t the time, and μ_e is the effective dynamic viscosity with $\mu_e = \mu + \mu_t$, μ the fluid viscosity and μ_t the turbulent viscosity. Note that the flow variables in Eqs. (1), (2) are filtered by the RNG procedure. In order to close the governing equations, the RNG k-ε two-equation formulations are adopted, with

$$\mu_t = C_\mu \frac{k^2}{\varepsilon} \tag{3}$$

where $C_\mu = 0.09$ is a theoretical model constant, and the time-dependent advection-diffusion equations for the turbulent kinematic energy k and its dissipation rate ε are

$$\frac{\partial \rho k}{\partial t} + \frac{\partial}{\partial x_j}[\rho (u_j - u_j^m) k] = \frac{\partial}{\partial x_j}\left(\frac{\mu_t}{\sigma_k}\frac{\partial k}{\partial x_j}\right) + \mu_t \left(\frac{\partial u_i}{\partial x_j} + \frac{\partial u_j}{\partial x_i}\right)\frac{\partial u_i}{\partial x_j} - \rho\varepsilon \tag{4}$$

$$\frac{\partial \rho \varepsilon}{\partial t} + \frac{\partial}{\partial x_j}[\rho (u_j - u_j^m) \varepsilon] = \frac{\partial}{\partial x_j}\left(\frac{\mu_t}{\sigma_\varepsilon}\frac{\partial \varepsilon}{\partial x_j}\right) + C_{1\varepsilon}\frac{\varepsilon}{k}\mu_t \left(\frac{\partial u_i}{\partial x_j} + \frac{\partial u_j}{\partial x_i}\right)\frac{\partial u_i}{\partial x_j} - \rho C_{2\varepsilon}\frac{\varepsilon^2}{k} \tag{5}$$

where the model constants $C_{1\varepsilon} = 1.42$, $C_{2\varepsilon} = 1.68$, $\sigma_k = 0.71942$ and $\sigma_\varepsilon = 0.71942$, which are derived theoretically, not based on the experimental calibrations, as is distinct from the widely used RANS model.

For a numerical wave flume, it is necessary to eliminate the reflection waves. An artificial damping force is hence introduced into the body force term in Eq. (2), which works as a physical spongy layer

$$f_i = g_i + R_i \tag{6}$$

where g_i is the gravitational acceleration, R_i is the artificial damping force. For the sake of the numerical stability, the damping force is only activated in the vertical direction for the present 2-D problem, which means that the horizontal component $R_x = 0$, while the vertical component R_y takes the following form[24]

$$R_y = -k_s \left(\frac{x - x_0}{D_s}\right)^2 \frac{y_b - y}{y_b - y_h} v \tag{7}$$

where x and y are the Cartesian coordinates of the grid nodes, x_0 is the coordinate at the start point of the spongy layer, v is the vertical velocity component, D_s is the total length of the damping zone in the direction of the wave propagation, y_b is the elevation of the seabed, y_h is the water depth and k_s is an empirical parameter determined by numerical tests.

The volume of fluid (VOF) method proposed is used to capture the free surface in this work. A fractional function of the VOF, denoted by φ, for a computational cell, is defined as

$$\varphi = 0 \quad \text{in air} \tag{8a}$$

$$\varphi = 0 < \varphi < 1 \quad \text{on the free surface} \tag{8b}$$

$$\varphi = 1 \quad \text{in water} \tag{8c}$$

The VOF function is governed by the advection equation

$$\frac{\partial \varphi}{\partial t} + (u_i - u_i^m)\frac{\partial \varphi}{\partial x_i} = 0 \tag{9}$$

In this work, the contour of the VOF function with $\varphi = 0.5$ is used to represent the interface between the water and air phases. In the computations, the fluid density and the effective viscosity are averaged by using the available VOF function

$$\rho = \varphi\rho_W + (1-\varphi)\rho_A, \quad \mu_e = \varphi\mu_{eW} + (1-\varphi)\mu_{eA} \tag{10}$$

where the subscripts W and A represent the water phase and the air phase, respectively.

The governing equations are solved based on the finite volume method implemented in the OpenFOAM package. The velocity and the pressure are separated by the pressure implicit with splitting of operators algorithm (PISO). The Euler method is used to discretize the transient term. The convection term and the diffusion term are discretized by the Gauss limited linear method and the Gauss linear corrected method, respectively. The details of the numerical implements in the OpenFOAM.

The numerical computations in this work always start from the still state, which allows the static water pressure and the zero velocity to be specified as the initial conditions. The no-slip boundary condition is imposed on the solid wall. At the upper boundary of the computational domain, a reference pressure $p = 0$ and a velocity condition $\partial \boldsymbol{u}/\partial \boldsymbol{n} = 0$ are implemented with $\boldsymbol{n}$ being the outward normal unit vector. The interface tension between the air and water phases is neglected in this work since the dynamic effects from the air phase are very small. At the two ends of the spongy layer, zero velocities are set in view of the fact that the waves are damped out there by the spongy layer.

During the computation, the time increment is automatically determined according to the Courant-Friedrichs-Lewy (CFL) condition

$$\Delta t = C_r \times \min\left(\frac{\sqrt{S_e}}{|u_e|}\right) \tag{11}$$

where S_e and $|u_e|$ are the area and the absolute velocity in a computational cell, respectively. The numerical tests of this work confirm that with $C_r = 0.5$, stable and accurate numerical results can be obtained.

1.2 *Potential flow model*

For the purpose of comparison, the conventional potential flow model is also used in this study. For the mass conservation of the incompressible and irrotational fluid flow, we have the following Laplace equation in terms of the velocity potential

$$\frac{\partial^2 \Phi(x,y,t)}{\partial x^2} + \frac{\partial^2 \Phi(x,y,t)}{\partial y^2} = 0 \tag{12}$$

where $\Phi(x,y,t)$ is the two-dimensional time and space dependent velocity potential, and x and y denote the horizontal and vertical coordinates, respectively. In the context of the linear and harmonic waves, the velocity potential can be separated to the time-dependent and spatial dependent parts, namely

$$\Phi(x,y,t) = \mathrm{Re}[-\mathrm{i}\omega\xi_j\phi_j(x,y)\mathrm{e}^{-\mathrm{i}\omega t}] \quad (j = 1,2,3) \tag{13}$$

where the operator $\mathrm{Re}[X]$ means the real part of the function X, (ξ_1, ξ_2) are the amplitudes of the body translation and $\xi_3 = \alpha_1$ the amplitude of the body rotation, ω is the angular frequency, and $\phi_j(x,y)$ stands for the complex spatial velocity potential corresponding to the unit body velocity in j direction, which satisfies also the Laplace equation in addition to the following boundary conditions

$$\frac{\partial \phi_j}{\partial y} = \frac{\omega^2 \phi_j}{g} \quad \text{on} \quad S_f \tag{14a}$$

$$\frac{\partial \phi_j}{\partial y} = n_j \quad \text{on} \quad S_b \tag{14b}$$

$$\frac{\partial \phi_j}{\partial y} = 0 \quad \text{on} \quad S_d \tag{14c}$$

$$\frac{\partial \phi_j}{\partial y} = \pm \mathrm{i}k\phi_j \quad \text{on} \quad S_r \tag{14d}$$

where S_f and S_b are the still water levels at $y = 0$ and at the body surface, respectively, n_1 and n_2 are the unit normal vector components of the body surface, $n_3 = (\boldsymbol{x} - \boldsymbol{x}_0) \times n$, and $\boldsymbol{x}_0$ is the coordinate of the rotational center, S_d is the sea bottom at $y = -h$ and S_r is the truncated radiation boundary.

The Laplace equation of the complex potential is solved by a higher order boundary element method. A

Table 1 Geometric dimensions of various edge configurations

	Sharp edge	Convex #1	Convex #2	Concave #1	Concave #2
Width, L_c /mm	0	18	27	18	27
Height, H_c / mm	0	9	18	9	18
Opening ratio, B_e / B_g *	1.0	0.8	0.7	1.2	1.3

*Note: With a constant moonpool width $B_g = 180$ mm, B_e the opening length

Rankin source and its image with respect to the seabed are adopted as the Green function

$$G(\boldsymbol{x}, \boldsymbol{x}_0) = \frac{1}{2\pi}(\ln r + \ln r_1) \tag{15}$$

where $\boldsymbol{x}(x, y)$ is a field point and $\boldsymbol{x}_0(x_0, y_0)$ is a source point, with $r = [(x - x_0) + (y - y_0)]^{1/2}$, $r_1 = [(x - x_0)^2 + (y + y_0 - 2h)^2]^{1/2}$. By using the second Green's theorem, a boundary integral equation can be obtained as

$$\alpha\phi_j - \iint_S \phi_j \frac{\partial G}{\partial n} \mathrm{d}S = -\iint_{S_b} n_j G \mathrm{d}S - \mathrm{i}k \iint_{S_c} G\phi_j \mathrm{d}S - \frac{\omega^2}{g} \iint_{S_f} G\phi_j \mathrm{d}S \tag{16}$$

where α is the solid angle coefficient. From the boundary integral equation, a linear system is obtained for the complex velocity potential

$$[A]_{N\times N}\{\phi_j\}_N = \{B\}_N \tag{17}$$

where N is the number of unknowns, $[A]$ the coefficient matrix and $\{B\}$ the right hand array. The wave elevation $\eta_j(x,t)$ in j direction is obtained as

$$\eta_j(x,t) = \mathrm{Re}[\zeta_j(x)\mathrm{e}^{-\mathrm{i}\omega t}] \quad (j = 1,2,3) \tag{18}$$

where $\zeta_j(x) = \omega^2 \xi_j \phi_j / g$ on S_f.

1.3 *Numerical setup and computational conditions*

A sketch for the numerical simulations is illustrated in Fig. 1. Two identical rectangular hulls, defined as the Hull A and the Hull B, respectively, are placed in a wave flume with a constant water depth h. A moonpool with the breadth B_g is formed by the two rigidly connected hulls. The breadth and the draft of the two hulls are denoted by B, d, respectively. An extremely large amplitude fluid resonance can be excited in the moonpool as the frequency of the motion of the hulls is close to the natural frequency of the confined fluid bulk. In the present numerical simulations, the displacements of the twin bodies are induced by the heaving motion

$$\xi_h(t) = A_b \sin(\omega t) \tag{19}$$

where A_b is the heaving amplitudes of the twin bodies. Two numerical sponge layers are arranged on the both ends of the wave flume in order to absorb the reflection waves. Four wave gauges are used to record the wave elevation, and they are located in the moonpool, the left side of the hull A and the right side of the hull B, respectively.

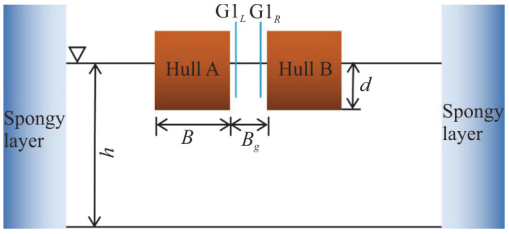

Fig. 1 (Color online) Numerical setup

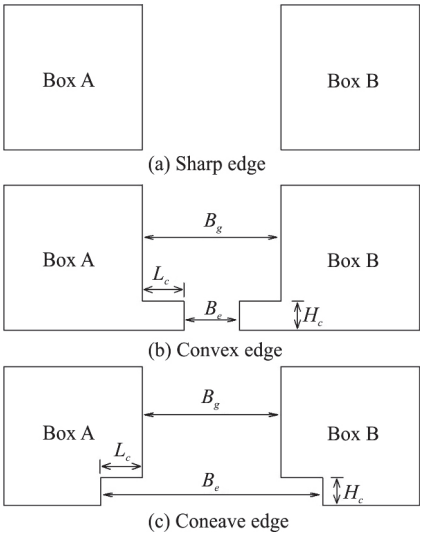

Fig. 2 Overview of edge configuration

Five edge profiles are considered in this work for

Table 2 Mesh resolution for convergency test

Edge profile		Mesh 1	Mesh 2	Mesh 3	Mesh 4	Mesh 5	Mesh 6
Sharp	Elements	2 140	4 820	8 188	18 300	32 672	72 800
	Nodes	4 580	10 098	16 968	37 490	66 534	147 378
Convex #1	Elements	2 262	4 639	8 288	18 600	33 072	73 694
	Nodes	4 838	9 728	17 182	38 114	6 7362	149 208
Convex #2	Elements	2 332	4 808	8 656	19 300	34 544	76 600
	Nodes	4 984	10 086	17 940	36 542	70 350	155 074
Concave #1	Elements	2 222	4 986	8 404	18 864	33 528	74 726
	Nodes	4 754	10 444	17 414	3 8642	68 274	151 272
Concave #2	Elements	2 252	5 116	17 876	19 364	34 302	76 208
	Nodes	4 818	10 714	8 628	39 662	69 846	154 266

the twin hulls, i.e., the sharp edge, the convex edges #1, #2, and the concave edges #1, #2. An overview of the different edge geometries is shown in Fig. 2. The edge profiles of the hulls are featured by their dimensions in length and height, denoted by L_c, H_c, respectively, and the geometric details are shown in Table 1. With the convex edges #1, #2 and the concave edges #1, #2, the total length of appendences or notches covers 20%, 30% of the moonpool width.

2. Numerical verifications and validations

The RNG based viscous numerical model is first validated against available experimental data. In accordance with the experiments conducted by Faltinsen et al.[3] and Fredriksen et al.[17], two hulls with the same breadth $B = 360$ mm are forced to perform the heave motion in a wave flume with the water depth $h = 1.03$ m. Both the moonpool draft d and width B_g are set to be 180 mm. The displacement of the twin hulls induced by the heaving motion is described by Eq. (19). Two wave gauges, $\mathrm{G1}_L$, $\mathrm{G1}_R$, in the moonpool are located 10 mm from each inside walls of the hulls, with their average values taken as the wave elevation results in the present work, defined as G1 in Fig. 1. The hulls are located at the middle of the computational domain. The left sponge layer covers the region from −10 m to −7 m while the right one ranges from 7 m to 10 m, with respect to the coordinate origin located at the moonpool center and the initial still water level.

2.1 *Mesh resolution test*

The numerical convergence is tested by four different meshes. Details of the mesh generations for various edge configurations are listed in Table 2. Typical mesh partitions in the vicinity of the hulls are shown in Fig. 3. In order to save computational time, non-uniform meshes are adopted. In general, square fine meshes with high resolution are adopted in the moonpool to account for the boundary layer effects and to accurately capture the large amplitude free surface oscillation. In the sponge layer, rectangular coarse meshes with large aspect ratio up to 1/20 (height/length) are adopted, which are used to dissipate the reflection wave.

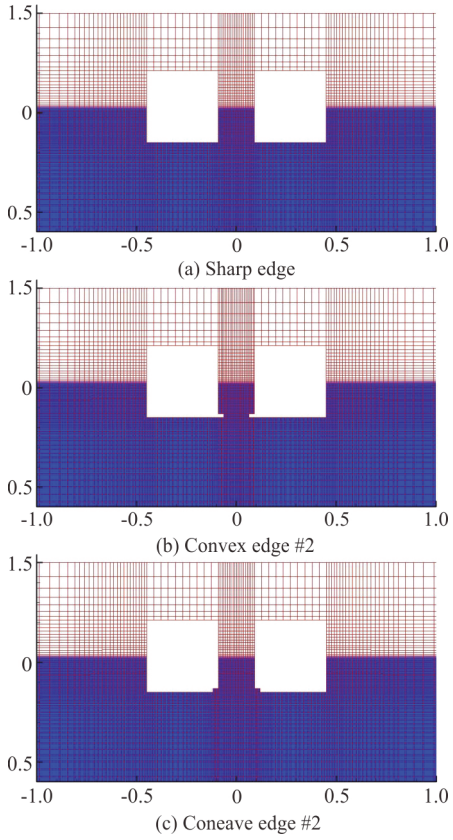

Fig. 3 (Color online) Typical computational meshes in the vicinity of hulls with different corner shapes

According to the experimental results of Faltinsen et al.[3], the dimensionless heaving frequency $\omega^2 B_g / g = 0.5$ corresponds to the most significant wave oscillation in the moonpool for the sharp edge profile. The numerical results of the wave amplitudes measured at the probe G1 are compared for various mesh resolutions in Fig. 4, for two forced

heaving amplitudes of $A_b = 5$ mm, 9.1 mm and for the five different edge geometries. The comparisons shown in Fig. 4 indicate that the change of the mesh density has little influence on the numerical results if N_n is larger than 3×10^4. Therefore, the mesh 3 can produce convergent solutions, and is used as the baseline for the computations in this work.

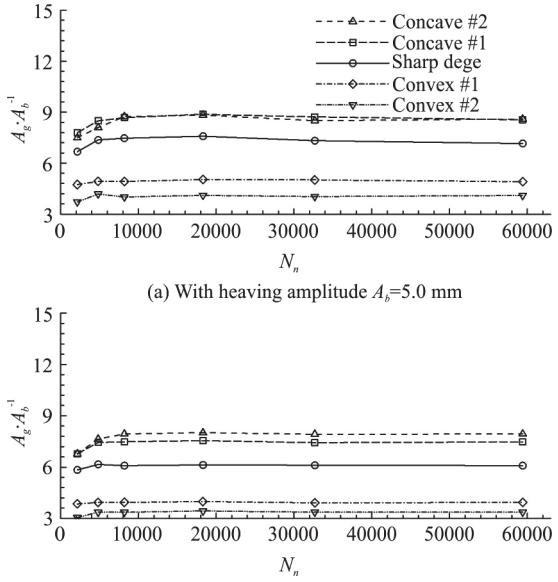

(a) With heaving amplitude A_b=5.0 mm

(b) With heaving amplitude A_b=9.1 mm

Fig. 4 Dimensionless amplitudes of free surface (A_g / A_b) at probe G1 (moonpool center) with different mesh resolutions ($h = 1.03$ mm, $B = 360$ mm, $d = B_g = 180$ mm, $\omega^2 B_g / g = 0.5$, N_n the number of computational nodes)

2.2 *Validation against heaving motion of twin hulls with sharp edge*

The numerical accuracy of the present turbulent wave model is validated against experimental data of Faltinsen et al.[3] for the twin hulls with sharp edge profiles. The variations of the wave elevations, including the mean wave amplitudes and the phase shifts, defined as A_g / A_b, φ_g at G1, against the heaving frequency $\omega^2 B_g / g$ are compared in Fig. 5. Two heaving amplitudes $A_b = 2.5$ mm, 5 mm are considered. For the purpose of comparisons, the numerical results obtained by the linear potential flow model are also presented.

Figure 5 shows that, for the two heaving amplitudes, the resonant frequencies of the fluid oscillation in the moonpool, predicted by the viscous fluid model and the potential flow model are almost identical to those observed in the experiments. The variation of A_g / A_b with $\omega^2 B_g / g$ in the moonpool, predicted by the present RNG turbulent model is found to be in good agreement with the experimental data. However, the potential flow model significantly over-predicts the free surface amplitude at G1 as the heaving frequencies are close to the resonant condition. The agreement between the present RNG model and the experimental phase shift in Fig. 5 is also quite well for both heaving amplitudes. As for the potential flow model, a little discrepancy with experimental results can be observed in G1.

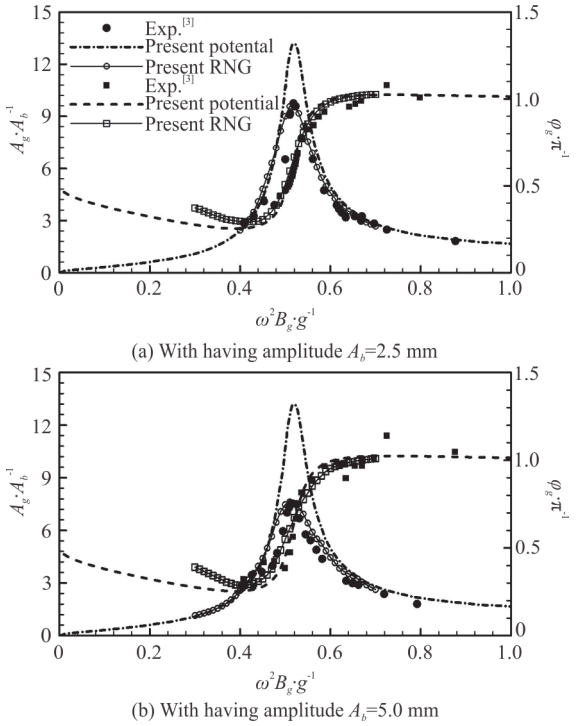

(a) With having amplitude A_b=2.5 mm

(b) With having amplitude A_b=5.0 mm

Fig. 5 Numerical validation and comparison of wave amplitude A_g and phase shift φ_g of G1 versus heaving frequency $\omega^2 B_g / g$ for twin hulls with sharp edge profile ($h = 1.03$ mm, $B = 360$ mm, $d = B_g = 180$ mm) under heaving amplitdues A_b = 2.5 mm, 5 mm

Further comparisons in Fig. 5 suggest that the relative resonant wave amplitudes in the moonpool with $A_b = 2.5$ mm obtained by the experiment and the viscous turbulent model are larger than those with $A_b = 5$ mm. This is related to the physical energy dissipations resulted from the viscous effects, which cannot be modeled correctly by the potential flow model. An opposite trend from the phase shift results can also be observed by Fig. 5, in which a little discrepancy for θ_g by various A_b can be observed in the moonpool.

The comparisons shown in Fig. 5 confirm that the present RNG based numerical wave flume performs well, and is capable of producing numerical

results in good agreement with the experimental data for various heaving frequencies and amplitudes. However, the potential flow model may over-predict the resonant response in the moonpool, as was also reported before by the other studies, for example, the gap resonance between fixed two or three boxes under water waves by Lu et al.[24], Moradi et al.[25-26] the resonant fluid oscillation in a moonpool by Faltinsen et al.[3], Fredriksen et al.[17].

2.3 *Validation against heaving motion of twin hulls with convex edge*

Comparisons and validations are also conducted for the convex edge profiles. The mean dimensionless wave amplitudes of A_g / A_b at G1 (located at the center of the moonpool) obtained by the present RNG turbulent model are compared in Fig. 6 with the measured data and the numerical results by Fredriksen et al.[17]. Note that the relative free surface amplitudes in Fig. 6 are given in a body-fixed non-inertial coordinate system as adopted in Fredriksen et al.[17]. Two edge sizes (#1, #2) and two heaving amplitudes of $A_b = 4.5$ mm, 9.1 mm are considered. Generally speaking, the present numerical results by using the RNG turbulent model are in agreement with the experimental observations and the numerical solutions by Fredriksen et al.[17]. However, small discrepancies between the two sets of numerical results are observed. This might be due to the differences between the two numerical models. The numerical simulations conducted by Fredriksen et al.[17] are based on a coupling computational method incorporating the potential flow model and the Navier-Stokes solver. As far as the modeling of viscous fluid flows is concerned, the viscous module of Fredriksen et al.[17] can be thought of a 2-D direct numerical simulation, which is, hence, expected to require very fine mesh resolution to identify the turbulent effects. Meanwhile, in their coupling model, only the flows in the lower region of the moonpool were simulated by the Navier-Stokes equations, while the upper region including the free surface was treated by the conventional potential flow model. As shown in Table 1, the convex edge #2 covers 30% of the moonpool width while the convex edge #1 covers 20% of the moonpool width. Theoretically, the smaller moonpool entrance of the convex edge of #2 with a larger heaving amplitude ($A_b = 9.1$ mm) is more likely to produce a stronger turbulence, giving rise to the smallest relative resonant amplitude in the moonpool. That is consistent with the results presented in Fig. 6(d). The turbulence is developed there and consequently the more significant energy dissipation has to be considered. As far as the cases with the same heave amplitude are concerned, for example, comparing Figs. 6(a), 6(c)/or Figs. 6(b), 6(d), it is shown that the change in the size of the convex edge has a limited influence on the resonant wave amplitude in the moonpool. However, the increase of the heaving amplitude (from 4.5 mm to 9.1 mm) in the cases with the same edge shape, the resonant

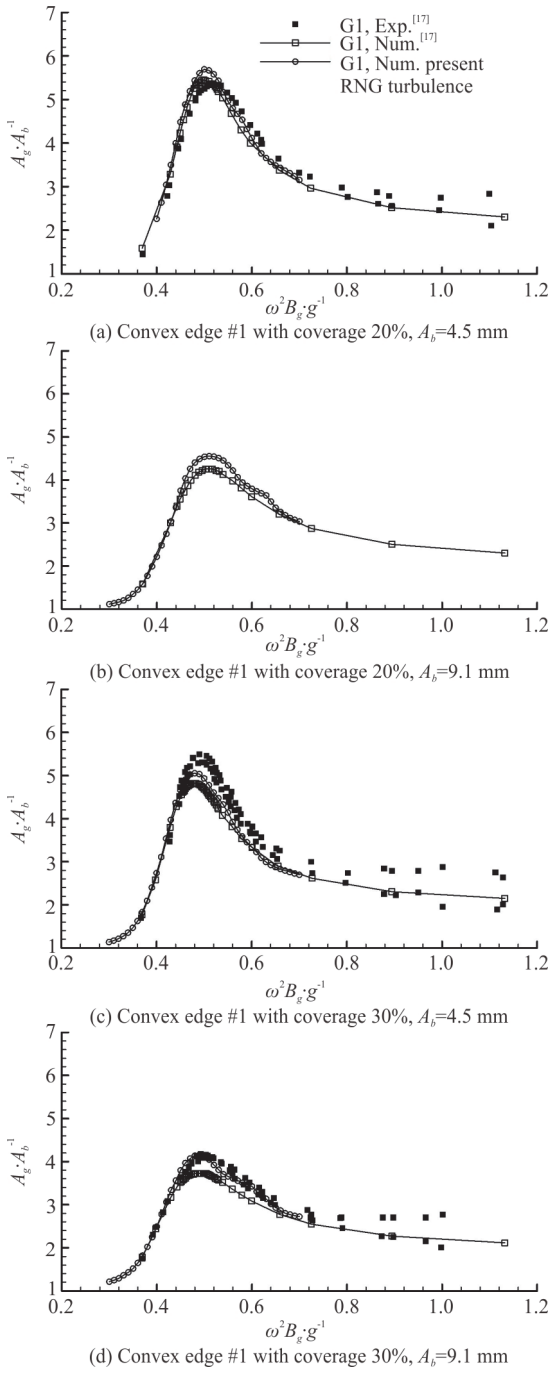

Fig. 6 Comparison of non-dimensional wave amplitudes in moonpool (A_g / A_b at G1) for different convex edges and heaving amplitudes ($h = 1.03$ mm, $B = 360$ mm, $d = B_g = 180$ mm. Note that the body-fixed reference system is used in this figure)

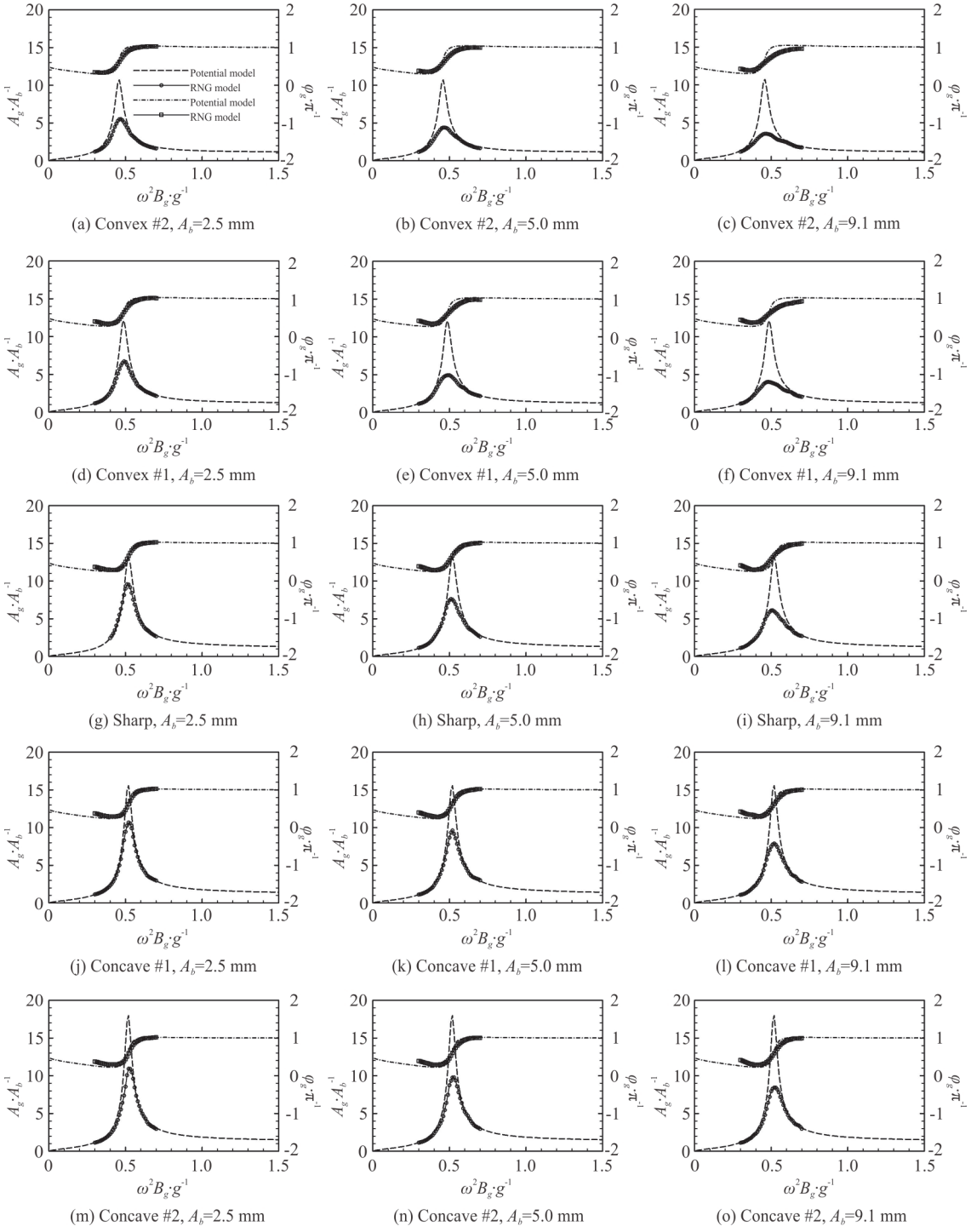

Fig. 7 Non-dimensional wave amplitudes $A_{g,r} / A_b$ with respect to heaving frequencies $\omega^2 B_g / g$ for different edge profiles

wave response decreases rapidly, which can be seen from the comparisons between Figs. 6(a), 6(b) or Figs. 6(c), 6(d). It seems that in the cases considered in Fig. 6 the heaving amplitude plays a more important role in controlling the resonant wave amplitude in the moonpool than the edge configuration.

3. Numerical results and discussions

The turbulent numerical wave flume validated above is employed to investigate the fluid resonance in the moonpool formed by two identical rectangular

hulls with different edge profiles under forced heaving excitations. The edge configurations considered here comprise the special cases of the concave profiles in addition to the previously checked sharp corners and convex corners. The detailed comparisons among the cases of concave, sharp and convex edges are to understand the vortex motion near the moonpool entrance and the turbulent effects on the flows in the moonpool. Moreover, the physical dissipations involved in the fluid resonance are expected to be closely related to the heaving amplitude. Therefore, numerical simulations with various amplitudes of heaving excitations, that is $A_b = 2.5$ mm, 5 mm and 9.1 mm, are conducted for comparison and analysis. In order to demonstrate the necessity of a viscous fluid model for the problem of the fluid resonance, the numerical results shown in the following figures also include the linear potential flow solutions. Three parts are included in the following section, namely, the general description of the wave response by the heaving motion, the influences of the edge configuration dependence of the heaving amplitude on the piston-modal resonant characteristics, and the examination of the flow pattern around the moonpool entrance. It should be mentioned here that the wave amplitudes presented in this section are evaluated in the space-fixed coordinate system.

3.1 *General description of wave response by heaving motion*

We start with the comparisons of the variations of the mean wave amplitudes in the moonpool (measured by the wave gauge G1 located in the moonpool, A_g / A_b) with the heaving frequency by the turbulent flow model and the potential flow model. In the numerical simulations, the ranges of the normalized heaving frequencies $\omega^2 B_g / g$ are from 0 to 1.5. The focus is on the piston-modal resonance that occurs in the moonpool induced by the heaving motion. As shown in Fig. 7, the piston-modal resonant frequencies predicted by the two numerical models are almost identical for each edge profile considered in this work. However, the potential flow model significantly over-predicts the resonant wave amplitude. This is because the physical energy dissipations cannot be correctly modeled by the conventional potential flow theory, in which the fluid flows are assumed to be in-viscid and irrotational. On the other hand, when the heaving frequencies are outside a certain band at either side of the resonant frequency, the potential flow model performs well. At these lower or higher frequencies, although the heaving amplitude keeps unchanged, the relatively small wave amplitude in the moonpool corresponds to a rather slow flow in the neighborhood of the moving bodies in the moonpool. And hence the viscous shear and turbulent dissipations are ignorable. The phase shifts φ_g at the gauge G1 have similar features for sharp and concave edges in Fig. 7, where the agreement of the results obtained by the potential flow model and the viscous flow model can be observed. Figure 7 shows that, for two convex edges (#1, #2), some discrepancies between the results obtained by the potential and viscous flow models can be observed around the resonant frequencies.

3.2 *Influence of edge configuration dependence of heaving amplitude on piston-modal resonant characteristics*

Special attention is paid to the influence of the edge configuration dependence of the heaving amplitude on the piston-modal resonant wave in the moonpool in the heaving motion. In order to clearly demonstrate that feature, the plots shown in Fig. 7 are re-arranged in Fig. 8. The numerical results obtained by the RNG model, as shown in Figs. 8(a)-8(c), suggest that, for a specific heaving amplitude, the edge configuration has three kinds of effects: (1) on the resonant wave height, (2) on the resonant frequency and (3) on the phase shift around the resonant frequency. Firstly, with the decrease of the opening size, that is, varying from the concave #2, the concave #1, the sharp edge, the convex #1 to the convex #2, the relative piston-modal resonant wave amplitude in the moonpool decreases. The maximal dimensionless resonant wave amplitude A_g / A_b can even reach 10.93, in the case of the concave #2 with the smallest heaving amplitude $A_b = 2.5$ mm in Fig. 12(c). While the minimal $A_g / A_b = 3.53$ is observed in the case of the convex #2 with the largest heaving amplitude of $A_b = 9.1$ mm in Fig. 12(a). Secondly, following the geometry sequence mentioned above, the piston-modal resonant frequency decreases, that is, the smaller the opening size the lower the resonant frequency. Similar variation tendencies are also observed in Fig. 12(d) for the numerical results by using the potential flow model. However, Fig. 15(d) suggests that the resonant frequencies in the first three cases, namely, the concave #2, the concave #1 and the sharp edge, are almost identical, as is different from the results predicted by the RNG turbulent model. As for the two convex edges, the potential flow model predicts also a smaller resonant frequency and a smaller resonant wave amplitude for a smaller opening size (the convex #2). Thirdly, the phase shift increases in the above geometry sequence around the piston-modal resonant frequency in the RNG model results. As for the potential model results, the phase shifts in the first three cases are nearly the same again,

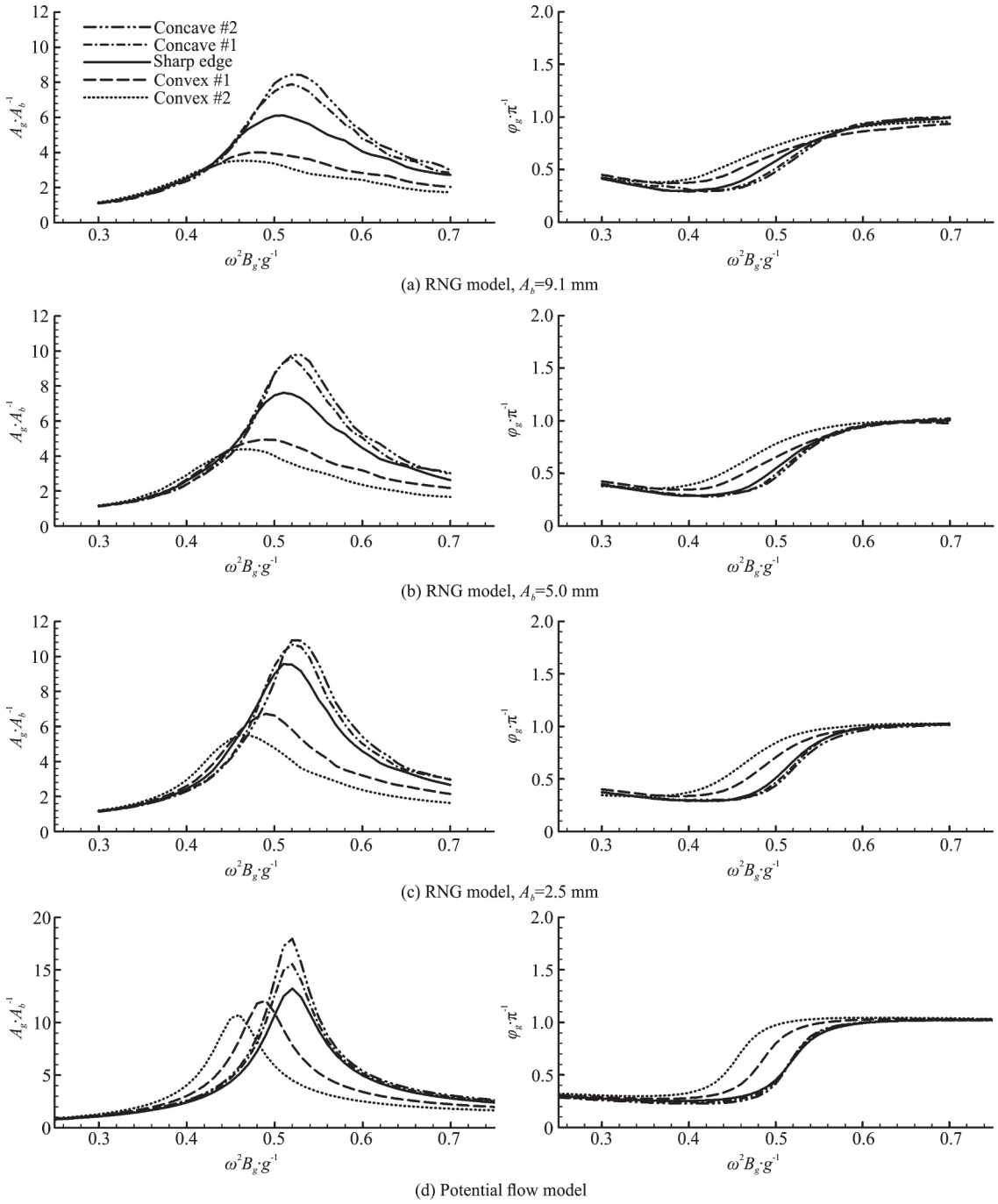

Fig. 8 Variation of wave amplitudes (left column) and phase shifts (right column) in moonpool (A_g / A_b) with heaving frequencies $(\omega^2 B_g / g)$ for various edge profiles

Table 3 Water volume entering into moonpool for various corner shapes under resonant conditions with $A_b = 5$ mm

Edge type	Opening ratio, B_e / B_g	Resonant frequency (period) $\omega^2 B_g / g$, T /s	Injected fluid volume, $\hat{\Delta}$ /m²	Resonant amplitude, A_g / A_b
Concave #2	1.3	0.53 (1.169)	0.0160	9.782
Concave #1	1.2	0.52 (1.180)	0.0157	9.620
Sharp edge	1.0	0.51 (1.192)	0.0120	7.617
Convex #1	0.8	0.49 (1.216)	0.0076	4.938
Convex #2	0.7	0.47 (1.241)	0.0068	4.387

while some discrepancy can be observed for the two convex edges. It is interesting to note that one sees very similar features for the resonant frequency and the phase shift around the piston-modal resonant frequency, in which the potential flow model predicts the same results for the concave #2, the concave #1 and the sharp edges. Moreover, detailed comparisons show that the phase shifts at the resonant frequencies are almost kept a value of $\pi/2$ rad for any heaving amplitude and edge profile.

It is believed that the piston-modal resonant wave amplitude is essentially controlled by the volume of the fluid entering into the moonpool from the moonpool entrance. To confirm this, the injected water volume during the half period, denoted by $\hat{\Delta}$, is evaluated as follows

$$\hat{\Delta} = \int_0^{T/2} \int_{x_s}^{x_e} v(x,t)\,\mathrm{d}x\mathrm{d}t \tag{20}$$

where x_s and x_e are the horizontal coordinates of the left and right ends of the entrance bottom, respectively, T the period of the heaving motion and $v(x,t)$ the vertical velocity component of the fluid flow. Note that the horizontal cross-section connecting x_s and x_e is attached to the heaving hulls, shown as a solid line S_1 in Fig. 9. By considering a typical heaving amplitude of $A_b = 5$ mm, the calculated data for the five edge configurations at their respective resonant conditions are listed in Table 3. It is shown that the injected water volume decreases gradually as the opening ratio of the moonpool entrance decreases, i.e., the larger the opening size, the larger the volume injected, as is consistent with the variation of the piston-modal resonant wave amplitude in the moonpool.

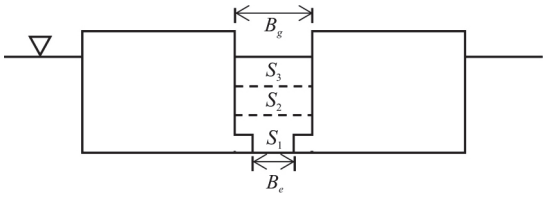

Fig. 9 Definition of typical cross-sections (solid line S_1 : Moving with heaving hulls, dashed lines S_2, S_3 : Space fixed, B_g, moonpool width, B_e width of moonpool entrance)

In addition to the cross-section S_1 defined as moving with the bottom entrance, the other two cross-sections fixed in space, i.e., S_2, S_3, shown by the blue dashed lines in Fig. 9, are also specified, which are, respectively, located at 0.09 m and 0.12 m lower than the initial still water level. Along these cross-sections, the average vertical velocities are evaluated. Firstly, the vertical flow velocity component $v(x,t)$ is averaged along the cross-section, which leads to a time-dependent space-averaged vertical velocity, namely, $\tilde{v}(t) = \int_{x_s}^{x_e} v(x,t)\,\mathrm{d}x/(x_e - x_s)$. Thus three space-averaged vertical velocities of $\tilde{v}_1(t)$, $\tilde{v}_2(t)$ and $\tilde{v}_3(t)$ can be obtained, which correspond to the three cross-sections of S_1, S_2 and S_3, respectively. Then the mean amplitude of $\tilde{v}(t)$ is further calculated by the formula $V = \int_{t_s}^{t_e} \tilde{v}(t)\,\mathrm{d}t/(t_e - t_s)$. Accordingly, the amplitudes of $\tilde{v}_1(t)$, $\tilde{v}_2(t)$ and $\tilde{v}_3(t)$ are denoted by V_1, V_2 and V_3, respectively, in this work. Figure 10 presents the comparisons of the time-series of $\tilde{v}_1(t)$, $\tilde{v}_2(t)$ and $\tilde{v}_3(t)$, together with the evolution of the free surface $\eta(t)$ in the moonpool, for various edge configurations at their resonant frequencies. First, the influence of the position of the space-fixed cross section on $\tilde{v}(t)$ is examined. As shown in Fig. 10 the velocities of $\tilde{v}_2(t)$ and $\tilde{v}_3(t)$, are the same. Further comparisons confirm that the ratios of the velocity amplitudes on S_2 and S_3 over that on S_1 are the same as the ratio of the moonpool width over the entrance width, that is

$$\frac{V_1}{V_2} = \frac{V_1}{V_3} = \frac{B_g}{B_e} \tag{21}$$

The coincidence between of $\tilde{v}_2(t)$ and $\tilde{v}_3(t)$ and the relation identified in Eq. (21) indicate clearly that the mass conservation is exactly guaranteed in the present RNG turbulent simulations.

The comparisons show that the velocities of the flow. i.e., $\tilde{v}_1(t)$, $\tilde{v}_2(t)$ and $\tilde{v}_3(t)$ are in phase while they are $\pi/2$ out of phase with the free surface displacement $\eta(t)$. When the free surface in the moonpool attains the maximum level, the flow velocities go nearly to zero. In view of the results in Fig. 10, the velocities of the flow are delayed a phase of $(2-\pi/2)$ phase with the heaving displacement of the hulls.

It is worth relating the parameters of the hull motion to those of the free surface oscillation in the moonpool. By assuming that the heaving motion and the fluid oscillation in the moonpool can be approximated by harmonic functions, the fluid volume entering the moonpool can be derived as follows

$$B_g\eta(t) = B_g A_g \sin(\omega t) = B_g \int V_2 \sin(\omega t)\mathrm{d}t =$$

$$-\frac{B_g V_2 \cos\omega t}{\omega} = \frac{B_g V_2 \sin(\omega t - \pi/2)}{\omega} \tag{22}$$

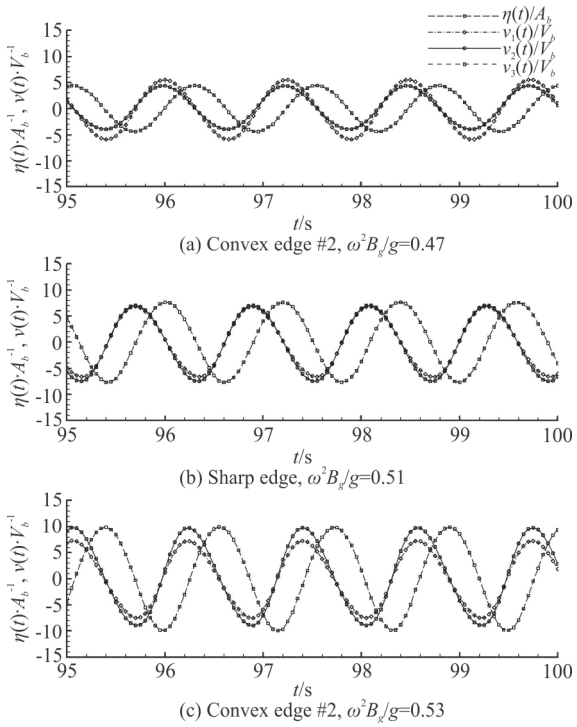

Fig. 10 Comparisons of time-series of mean vertical velocities and free surface oscillations in moonpool for various edge profiles (A_b = 5 mm)

With Eq. (22) in mind, i.e., $V_2 = V_3 = V_1 B_e / B_g$, the above formula can be rewritten as

$$B_g A_g = \frac{B_g V_2}{\omega} = \frac{B_g V_3}{\omega} = \frac{B_g V_1 B_e}{\omega B_g} \Leftrightarrow$$

$$A_g = \frac{V_2}{\omega} = \frac{V_3}{\omega} = \frac{B_e V_1}{\omega B_g} \tag{23}$$

Since the heaving motion follows a harmonic function, we immediately obtain that $V_b / A_b = \omega$. Inserting it into Eq. (23), we have

$$A_g = \frac{V_2 A_b}{V_b} = \frac{V_3 A_b}{V_b} = \frac{B_e V_1 A_b}{B_g V_b} \Leftrightarrow$$

$$\frac{A_g}{A_b} = \frac{V_2}{V_b} = \frac{V_3}{V_b} = \frac{B_e V_1}{B_g V_b} \tag{24}$$

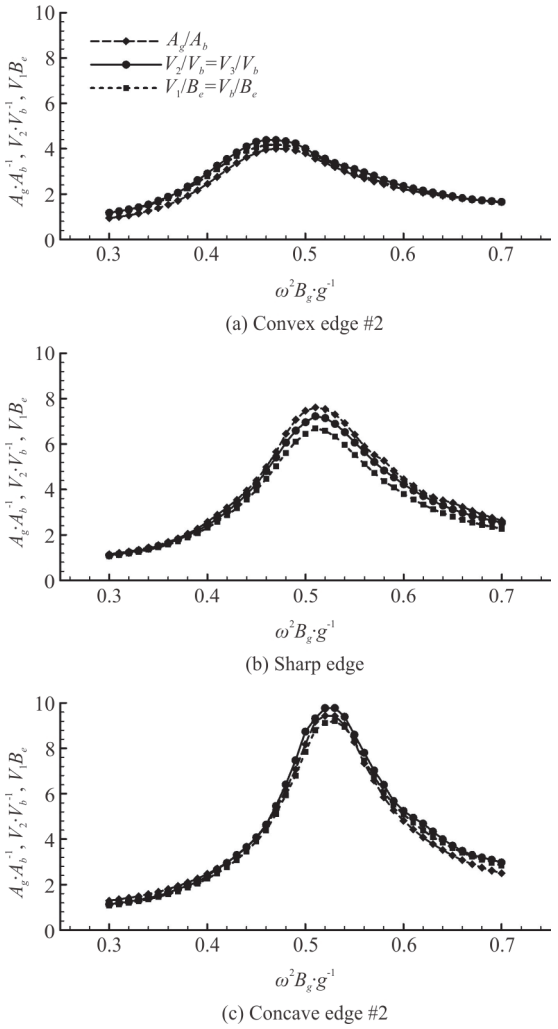

Fig. 11 Dependence of non-dimensional wave amplitudes in the moonpool on the non-dimensional vertical velocity components for A_b = 5 mm

The predictions by Eq. (24) are confirmed by Fig. 11 based on the numerical results of the present RNG turbulent model, where the variations of the non-dimensional amplitudes of A_g / A_b, V_2 / V_b and $V_1 B_e / V_b B_g$ with the heaving frequency are compared for various edge configurations. It is shown that the three curves for each edge profile are almost identical. The maximal relative error, with respect to the case of the sharp corner, is less than 5.73%. The slight difference might be due to the complex vortical flows around the moonpool entrance, with the vertical flow component deviating from the exact harmonic oscillation. The relationship presented in Eq. (24) and confirmed by Fig. 11 suggests that if the vertical velocity amplitude V_1 along the moonpool entrance is known, the resonant wave height in the moonpool can be readily estimated. Certainly it is not an easy

task to determine the injecting velocity since it is highly related to the edge configuration and implicitly associated with the local flow and pressure fields. However, one does see the possibility to approximate the piston-modal resonant wave amplitude by using an iterative procedure with the aid of an appropriate damping term for the potential flow model.

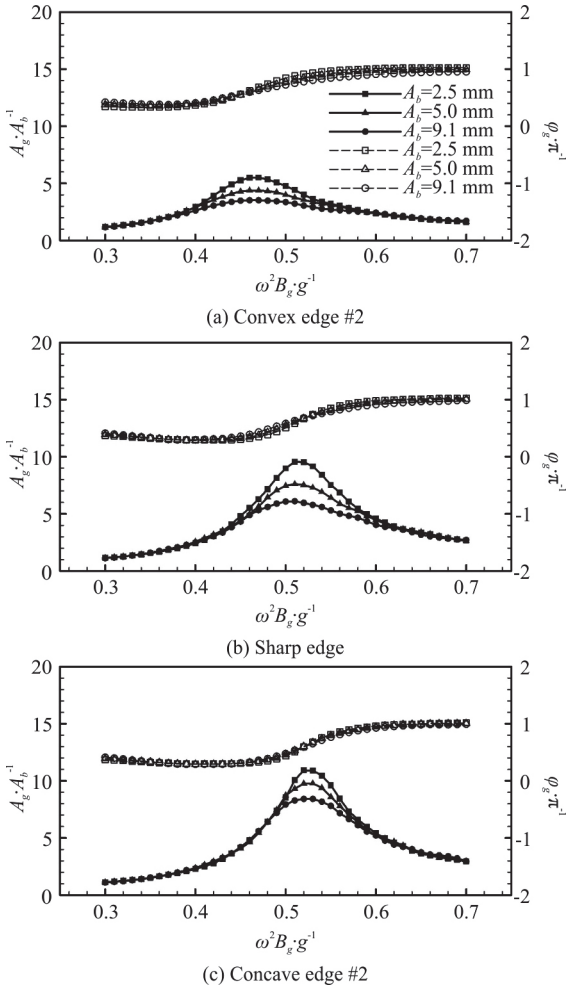

Fig. 12 Comparisons of non-dimensional wave amplitudes (left column) and phase shifts (right column) in moonpool (G1 probe) under various forced heaving amplitudes

The piston-modal resonant wave amplitude in the moonpool is also affected by the heave amplitude in addition to the edge configuration discussed above. The variations of the relative amplitude in the moonpool (A_g / A_b) with the exciting frequency at various heaving amplitudes are compared in Fig. 12. As far as a specific corner shape is concerned, it can be found that a larger heaving amplitude leads to a smaller relative wave amplitude in the moonpool around the resonant frequency. This is because the increase of the heaving amplitude enhances significantly the damping effect. However, as the exciting frequency deviates from the resonant frequency within a certain range, the influence of the heaving amplitude can be observed to be diminished. The numerical results shown in Fig. 12 indicate also that the piston-modal resonant frequency is hardly affected by the heaving amplitude/or the resonant amplitude in the moonpool. Unlike the observations of the wave amplitudes in the moonpool, the relative radiation wave seems having rather limited dependence on the forced heaving amplitude. Figure 12 also shows that, for the phase shift in the moonpool, the heaving amplitude effect is more and more important with the decrease of the opening size (varying from the concave #2, the concave #1, the sharp edge, the convex #1 to the convex #2). The phase shift results for various heaving amplitudes nearly coincide in the case of the concave #2 in Fig. 12(e), while they are different when $\omega^2 B_g / g$ is larger than 4.6 (the resonant frequency) in the case of the convex #2 in Fig. 12(a).

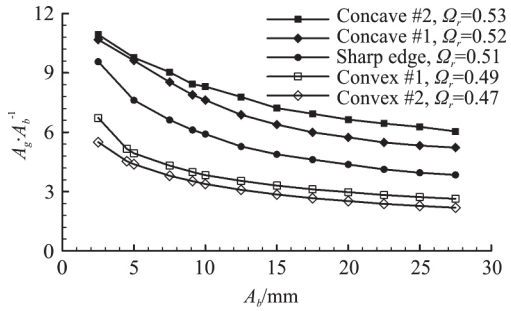

Fig. 13 Variation of resonant wave amplitudes with heaving amplitudes for various edge configurations

Under the piston-modal resonant conditions, the dependence of the wave amplitude in the moonpool on the heaving amplitude is further investigated by considering a wide range of amplitudes up to $A_b =$ 27.5 mm . The resonant conditions adopted in Fig. 13 are based on the identifications of Fig. 12 with a heaving amplitude of $A_b = 5$ mm , and are denoted by Ω_r in terms of the dimensionless parameter $\omega^2 B_g / g$. Figure 13 shows that the relationship between the resonant amplitude and the heaving amplitude is not linear. The least square fitting results suggest an approximate power function of $A_g = \kappa - \gamma A_b^{0.3}$. However, the free parameters κ, γ vary much for different edge shapes. It implies a complicated dependence of the piston-modal resonant amplitude in the moonpool on the heaving amplitude of the floating body and the configuration of the moonpool entrance. And both the heaving amplitude and the edge shape are closely related to the local flow pattern. The me-

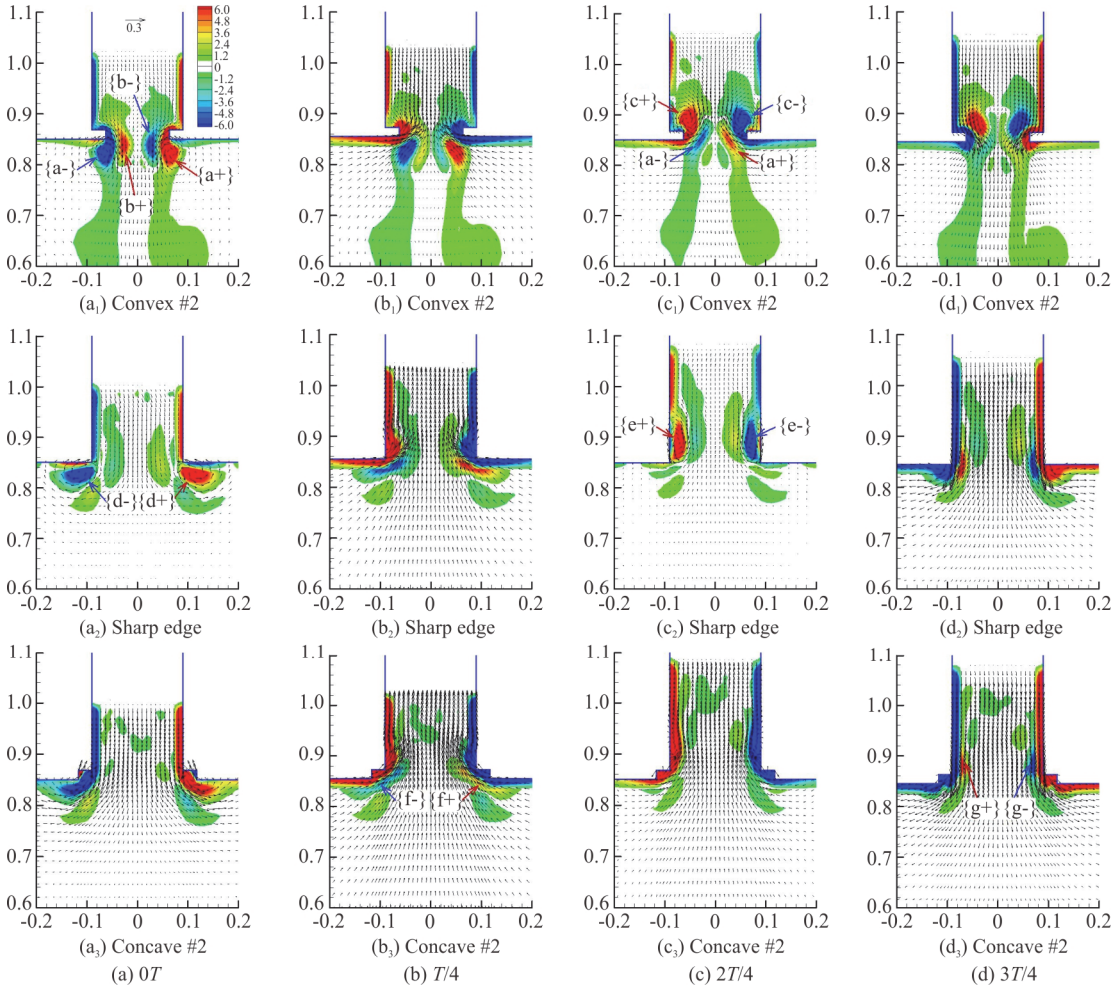

Fig. 14 (Color online) Velocity fields and vortices contours of piston-mode resonance in the near region of gap entrance during one period of heaving motion (under resonant conditions and $A_b = 5$ mm) (First row: Convex #2, Second row: Sharp edge, Third row: Concave edge #2. Note that the uniform scales of velocity and vortices are used in this figure)

chanical energy dissipation may play an important role in controlling the resonant amplitude, due to the flow separation from the moonpool entrance, the wall shear stress and the internal friction generated by the advection and the diffusion of the vortices.

3.3 *General description of wave response by heaving motion*

The flow field in the vicinity of the moonpool is investigated, to understand the physical dissipation involved in the fluid resonance. Three typical corner configurations are considered, namely, the convex #2, the sharp corner and the concave #2. The velocity vector together with the vortex contour for the three corner shapes are depicted in Fig. 14 under their respective resonant conditions of $\Omega_r = \omega^2 B_g / g =$ 0.47, 0.51 and 0.53 for the piston-modal resonance. The numerical results of Fig. 14 are based on a uniform heaving amplitude $A_b = 50$ mm. The first, second and third rows are arranged in the sequence corresponding to the convex #2, the sharp corner and the concave #2.

Roughly speaking, three typical flow modes can be identified in Fig. 14 corresponding to the three edge configurations. For the convex edge configuration, it is observed that, at the beginning of one period heaving motion, there are two pairs of vortices developed around the moonpool entrance. And each pair comprises two vortices with opposite sign. With the flow vector, one vortex structure (a^- or a^+) is clearly identified below each appendence, while the other vortices (b^+ or b^-) are from the strong flow shear, without a clear vortex structure identified by the flow vectors. Along the side walls inside the moonpool, obvious shear layers are observed. Meanwhile, in the flow domain below the heaving hulls, a large region is occupied by the vortical flows. With the time elapse, the vortex pair (a^- or a^+)

propagates into the moonpool as the bodies move upward, while the vortex pair (b^+ or b^-) dissipates gradually. At $t = 2T/4$, the former vortices b^+ and b^- are almost dissipated out, and a new pair of vortex bubbles (c^+, c^-) develops clearly at the inner corner of the moonpool. The previously observed vortices a^-, a^+ move to the near position occupied by b^+ and b^-, respectively. In the following half period, an inverse procedure is observed, and the initial flow scenery at $0T$ finally reappears at T. The numerical results for the convex #2 edge shape suggest a three-pair (3P) vortex mode near the moonpool entrance.

The second row of Fig. 14 presents the flow evolution around the sharp corner. Similar to the observations of the convex #2, two attached vortex structures, i.e., d^- and d^+, are formed, respectively. But they are totally below the two body ends, implying a phase lag in the vortex evolution compared with the previous case of the convex #2. And, the concomitant secondary vortices with inverse signs (namely, the counterparts of b^- and b^+ for the convex edge) are absent. During the first half period of the heaving motion, the attached vortices d^- and d^+ move towards and enter the moonpool, and finally emerge with the secondary shear layer in the moonpool. At $t = 2T/4$, two new vortices are formed in the moonpool, i.e., e^+ and e^-. It should be noted here that the vortices e^+ and e^- are not originated from the previously developed d^- and d^+, but independently developed from the inner wall shear layer. Therefore, two pairs of vortices are developed for the sharp corner shape during one period of the heaving motion, which is defined as the 2P vortex mode in this work. Again, a strong flow shear is observed along the solid wall. However, comparing with the case of the convex #2, the vortical flows below the heaving hulls are not as significant as before.

Looking at the third row of Fig. 14 for the concave #2 edge shape, one may observe that the overall flow pattern is somewhat similar to that observed for the sharp corner. However, at the instant of $0T/4$, the velocity vectors are not clearly in isolated vortex structures at the end bottom of the hulls. The strong shear layers along the moonpool wall are well developed, and extend to surround the moonpool ends. At $T/4$, due to the reversion of the flow direction, two small visible vortices, f^+ and f^-, appear below the end bottoms. Meanwhile the sign of the vortex distribution along the side wall of the moonpool changes. However, the two vortices are dissipated rapidly and disappear at $2T/4$. After that, two very small vortices g^+ and g^- are observed in the moonpool at $3T/4$, they are also dissipated rapidly. It can be said that the flow field for the concave #2 is mainly characterized by the shear layers, with a rather weak vortex motion. Due to the fact that the observed two pairs of vortices dissipate so fast and develop with a phase lag of $T/4$ as compared with the barge heaving displacement, the corresponding flow mode for the concave edges is named the shear dominated and weak delayed 2P mode. Comparing with the previous two edge configurations, the velocity magnitude, both in and below the moonpool, increases substantially, which accounts for the largest amplitude of the wave motion in the moonpool.

In general, for the three edge configurations considered in Fig. 14, no significant vortex shedding is observed although the attached vortex structures are developed. This might be due to the relatively small amplitude and period of the heave motion under the concerned resonant conditions. It is reasonable to expect that with the increase of the KC number ($v_b T/l$, with l being a characteristic length), fully developed vortices may finally shed from the body surface. From the flow fields, it is shown that with the convex edge shape, the most significant vortical flow is generated while the concave edge leads to, the weakest one. This can account for the physical dissipation qualitatively. The dissipation rate (the energy dissipation per unit volume and unit time) of the viscous fluid flow can be described by $\Psi = 2\mu s_{ij} s_{ij}$, where $s_{ij} = 0.5(u_{i,j} + u_{j,i})$ is the strain rate tensor, and μ the dynamics viscosity. For the present two-dimensional incompressible flow, it can be simplified to $\Psi = \mu[(v_{,x} - u_{,y})^2] + 4\mu(u_{,y} v_{,x} - u_{,x} v_{,y})$. The first term, related to the enstrophy ($\varpi = \omega_i \omega_i$, the square of vortices), plays the most important role in the mechanical energy dissipation for a wall bounded region, while the other terms make a limited contribution. That means that the more significant the vortical flow (e.g., in the convex edge), the more the dissipations are involved in the resonance, leading to the smaller relative wave amplitude A_g / A_b in the moonpool, which is indeed consistent with the numerical results of this work.

4. Conclusions

2-D turbulent simulations are carried out in this work to investigate the piston-modal resonance in a confined moonpool formed by two identical rectangular hulls in in-phase heaving motions. The numerical wave flume is developed based on the

OpenFOAM package by using the RNG turbulent model and the VOF interface capture technique. After numerical verifications and validations against experimental data, the influences of the edge configuration of the moonpool entrance and the heaving amplitude of the rectangular hulls on the resonant responses in the moonpool are examined and compared with the numerical results of the conventional potential flow model. Five edge configurations, including the two concave corners, two convex corners and a sharp corner, are considered in this work. Theoretical analysis based on the mass conservation and the generalization of the turbulent flow pattern around the moonpool entrance are also presented in this study.

The numerical investigation results suggest that the edge configurations near the moonpool entrance have a significant influence on the piston-modal resonance in the moonpool. With the increase of the opening size (i.e., varying from the convex edge to the sharp edge and to the concave edge in this work), the resonant frequency and the resonant wave amplitude increase. The increase of the resonant amplitude can be explained by the fluid volume (mass) injected into the moonpool. More fluid bulk injected into the moonpool per half period of the hull oscillation for a wider moonpool entrance leads to a higher resonant wave height. The piston-modal resonant wave height in the moonpool is further related to the heaving amplitude of the hulls, the flow velocity in the moonpool and the geometric dimensions of the moonpool entrance based on the principle of the mass conservation. An approximated formula is derived, which shows a good agreement with the numerical solutions obtained by using the RNG turbulent model.

The potential flow model can be used to predict the piston-modal resonant frequencies, but the resonant wave height is over-predicted due to its inherent feature by ignoring dissipations. With the increase of the heaving amplitude, the flow velocity in the moonpool increases, which leads to more significant dissipations. And hence the difference between the potential flow model and the turbulent model becomes evident, and the relative wave amplitude in the moonpool decreases. A general power function might be utilized to describe the decrease of the piston-modal resonant wave amplitude with the heaving amplitude. However, the free parameters involved in the power function are found to be highly dependent on the edge configurations, indicating a complicated dependence of the resonant wave height on the edge configuration. The present numerical simulation results show that the heaving amplitude hardly affects the piston-modal resonant frequency, with only a slight decrease of the resonant frequency being observed.

The flow field results indicate that the edge configuration can substantially change the flow pattern around the moonpool entrance for the piston-modal resonance in the heaving motion. The three-pair (3P) vortex mode can be identified for the convex edge. While the sharp edge features the two-pair (2P) vortex mode. The flow field of the concave edge is found to be mainly dominated by the boundary shear. The vortex formation and development is not significant. Therefore, it leads to the shear dominated and weak delayed 2P mode. In the scope of this work, the numerical simulations do not identify notable vortex shedding from the moonpool corners. The present turbulent flow analysis can reveal the dissipative effects, as is important in the physical mechanism that controls the resonant wave response in the moonpool.

Acknowledgements

This work was supported by the Pre-research field Fund Project of the Central Military Commission of China (Grant No. 61402070201), the Fundamental Research Funds for the Central Universities (Grant No. DUT18LK09, DUT2017TB05). The authors gratefully acknowledge the Supercomputer Center of Dalian University of Technology for providing computing resources.

References

[1] Saitoh T., Miao G. P., Ishida H. Theoretical analysis on appearance condition of fluid resonance in a narrow gap between two modules of very large floating structure [C]. *Proceedings of the Third Asia-Pacific Workshop on Marine Hydrodynamics*, Shanghai, China. 2006, 170-175.

[2] Peric M., Swan C. An experimental study of the wave excitation in the gap between two closely spaced bodies, with implication for LNG offloading [J]. *Applied Ocean Research*, 2015, 51: 320-330.

[3] Faltinsen O. M., Rognebakke O. F., Timokha A. N. Two-dimensional resonant piston-like sloshing in a moonpool [J]. *Journal of Fluid Mechanics*, 2007, 575, 359-397.

[4] Sun L., Eatock Taylor R., Taylor P. H. Wave driven free surface in the gap between a tanker and an FLNG barge [J]. *Applied Ocean Research*, 2015, 51: 331-349.

[5] Feng X., Bai W. Wave resonance in a narrow gap between two barges using fully nonlinear numerical simulation [J]. *Applied Ocean Research*, 2015, 50: 119-129.

[6] Li Y., Zhang C. Analysis of wave resonance in gap between two heaving barges [J]. *Ocean Engineering*, 2016, 117: 210-220.

[7] Lu L., Teng B., Cheng L. et al. Modelling of multi-bodies in close proximity under water waves – Fluid resonance in narrow gaps [J]. *Science China Physics, Mechanics and Astronomy*, 2011, 54(1): 16-25.

[8] Lu L., Teng B., Sun L. et al. Modelling of multi-bodies in close proximity under water waves–Fluid forces on floating bodies [J]. *Ocean Engineering*, 2011, 38(13): 1403-1416.

[9] Liu Y., Li H. J. A new semi-analytical solution for gap resonance between twin rectangular boxes [J]. *Journal of Engineering for the Maritime Environment*, 2014, 228(1): 3-16.

[10] Lu L., Cheng L., Teng B. et al. Numerical simulation and comparison of potential flow and viscous fluid models in near trapping of narrow gaps [J]. *Journal of Hydrodynamics*, 2010, 22(5Suppl.): 120-125.

[11] Li X., Xu L. Y., Yang J. M. Study of fluid resonance between two side-by-side floating barges [J]. *Journal of Hydrodynamics*, 2016, 28 (5): 767-777.

[12] Gao J., Zang J., Chen L. et al. On hydrodynamic characteristics of gap resonance between two fixed bodies in close proximity [J]. *Ocean Engineering*, 2019, 173: 28-44.

[13] Yang S. H., Kwon S. H. Experimental study on moonpool resonance of offshore floating structure [J]. *International Journal of Naval Architecture and Ocean Engineering*, 2013, 5(2): 313-323.

[14] Zhao W., Wolgamot H. A. Taylor P. H. et al. Gap resonance and higher harmonics driven by focused transient wave groups [J]. *Journal of Fluid Mechanics*, 2017, 812: 905-939.

[15] Zhu H. R., Zhu R. C., Miao G. P. A time domain investigation on the hydrodynamic resonance phenomena of 3-D multiple floating structures [J]. *Journal of Hydrodynamics*, 2008, 20(5): 611-616.

[16] Elie B., Reliquet G., Guillerm P. E. et al. Simulation of the gap resonance between two rectangular barges in regular waves by a free surface viscous flow solver [C]. *The 32nd International Conference on Ocean, Offshore and Arctic Engineering*, Nantes, France, 2013.

[17] Fredriksen A. G., Kristiansen T., Faltinsen O. M. Experimental and numerical investigation of wave resonance in moonpools at low forward speed [J]. *Applied Ocean Research*, 2014, 47: 28-46.

[18] Kristiansen T. Faltinsen O. M. A two-dimensional numerical and experimental study of resonant coupled ship and piston-mode motion [J]. *Applied Ocean Research*, 2010, 32: 158-176.

[19] Jiang S. C., Bai W., Tang G. Q. Numerical simulation of wave resonance in the narrow gap between two non-identical boxes [J]. *Ocean Engineering*, 2018, 156: 38-60.

[20] Jiang S. C., Bai W., Cong P. W. et al. Numerical investigation of wave forces on two side-by-side non-identical boxes in close proximity under wave actions [J]. *Marine Structures*. 2019, 63: 16-44.

[21] Jiang S. C., Bai W., Tang G. A. Numerical investigation of piston-modal wave resonance in the narrow gap formed by a box in front of a wall [J]. *Physics of Fluids*, 2019, 31: 052105.

[22] Tan L., Lu L., Tang G. Q. et al. A viscous damping model for piston mode resonance [J]. *Journal of Fluid Mechanics*, 2019, 871: 510-533.

[23] Kristiansen T. Faltinsen O. M. Application of a vortex tracking method to the piston-like behavior in a semi-entrained vertical gap [J]. *Applied Ocean Research*, 2008, 30: 1-16.

[24] Lu L., Cheng L., Teng B. et al. Numerical investigation of fluid resonance in two narrow gaps of three identical rectangular structures [J]. *Applied Ocean Research*, 2010, 32 (2): 177-190.

[25] Moradi N., Zhou T., Cheng L. Effect of inlet configuration on wave resonance in the narrow gap of two fixed bodies in close proximity [J]. *Ocean Engineering*, 2015, 103: 88-102.

[26] Moradi N., Zhou T., Cheng L. Two-dimensional numerical study on the effect of water depth on resonance behavior of the fluid trapped between two side-by side bodies [J]. *Applied Ocean Research*, 2016, 58: 218-231.